

Accurate internuclear potential energy functions for the ground electronic states of NeH^+ and ArH^+



John A. Coxon^a, Photos G. Hajigeorgiou^{b,*}

^a Department of Chemistry, Dalhousie University, Halifax, Nova Scotia B3H 4J3, Canada

^b Centre for Primary Care and Population Health, School of Medicine, University of Nicosia, 21 Iliia Papakyriakou, Engomi, P.O. Box 24005, 1700 Nicosia, Cyprus

ARTICLE INFO

Article history:

Received 15 May 2016

In revised form 22 July 2016

Accepted 1 August 2016

Available online 2 August 2016

Keywords:

Direct-potential-fit

Rare gas hydride cations

NeH^+

ArH^+

Potential energy functions

Born-Oppenheimer breakdown

ABSTRACT

All pure rotational and vibrational-rotational spectroscopic line positions available on the ground $X^1\Sigma^+$ electronic states of the rare gas hydride cations NeH^+ and ArH^+ have been employed in weighted least-squares direct fits to the potential energy functions, together with auxiliary functions describing breakdown of the Born-Oppenheimer approximation. All radial functions are represented by compact analytical models, and the spectroscopic line positions are reproduced to within the associated experimental uncertainties by the quantum-mechanical eigenvalues of the derived Hamiltonians. The potential energy functions are constrained to approach the theoretical radial behavior at long-range. Accurate vibrational term values and rotational and centrifugal distortion constants are provided for all stable isotopologues of NeH^+ and ArH^+ included in the least-squares fits.

© 2016 Elsevier Inc. All rights reserved.

1. Introduction

The concept of a potential energy function (PEF) for a diatomic molecular system is supported by the Born-Oppenheimer (BO) or clamped-nuclei approximation [1]. The ansatz rests on the large ratio of the nuclear to electronic masses, and assumes that the electronic cloud distribution around the binuclear structure adjusts instantaneously to small finite nuclear motions. The concept of a PEF also survives the next level of sophistication, known as the adiabatic approximation [2], with diagonal radial corrections added to the BO potential, and computed as the expectation values of the nuclear kinetic energy operator over the electronic wavefunctions. When nuclear motions become significant relative to the adjustment of the electronic distribution, the adiabatic approximation breaks down. Highly energetic rotations and vibrations couple adiabatic states of appropriate symmetry, and it is then necessary to account for nonadiabatic corrections to the eigenvalues of the state under consideration. In the strict theoretical context of nonadiabatic theory, only energy levels can be calculated, and the concept of a nonadiabatic PEF is not considered valid. On the other hand, several investigators [3–6] have shown that it is possible to perform a van Vleck transformation of the nonadiabatic Hamiltonian operator, projecting off-diagonal elements onto separate effective radial functions that modify both the rotationless PEF

and the rotational energy operator. In this fashion, the concept of an effective nonadiabatic PEF has been increasingly accepted, especially in direct-potential-fit (DPF) applications.

Adiabatic and nonadiabatic correction terms arising from the two atomic centers are inversely proportional to the masses of the constituent atoms. Thus, lighter diatomic systems, such as hydrides and lithium-containing molecules, form appropriate cases for investigating significant BO breakdown effects. Over a decade ago, the ground electronic states of four isotopologues of the helium hydride cation, HeH^+ , were the subject of a DPF analysis [7] that yielded the BO PEF and radial functions describing adiabatic and nonadiabatic effects. A recent *ab initio* study [8] on HeH^+ has shown that, as for H_2 , modern theoretical methods are capable of approaching spectroscopic accuracy, for two-electron systems. For heavier many-electron systems, however, the DPF method is still the method of choice in deriving PEFs that are fully consistent with the spectroscopic line positions within the experimental measurement uncertainties.

In the present work, we undertake DPF analyses employing all spectroscopic data available on the ground electronic states of NeH^+ and ArH^+ . Since these systems are isovalent with the hydrogen halides, they possess $^1\Sigma^+$ ground electronic states. In terms of isotopic substitution, neon has two stable isotopes with substantial natural abundance, ^{20}Ne and ^{22}Ne , and argon has three stable isotopes, ^{36}Ar , ^{38}Ar , and ^{40}Ar . The low (0.27%) natural abundance of ^{21}Ne has been an obstacle to observation of any spectral transitions for diatomic species containing this isotope. Combined with ^1H and

* Corresponding author.

E-mail address: Hajigeorgiou.p@unic.ac.cy (P.G. Hajigeorgiou).

Table 1
Comparison of the present study with similar previous studies on ArH⁺ ^a.

Ref.	DS	JDNE	LRF	QMP	EU
Present study	+	+	+	+	+
Ref. [10]	–	+	–	+	+
Ref. [11]	–	+	–	–	–
Ref. [12]	–	–	+	+	+
Ref. [13]	–	–	+	+	+
Ref. [14]	–	+	–	+	+
Ref. [15]	–	+	–	+	+
Ref. [16]	–	–	–	–	–
Ref. [17]	–	+	–	+	+

^a DS = Use of the complete data set. JDNE = Inclusion of *J*-dependent nonadiabatic effects. LRF = Correct long-range functional form. QMP = Use of an exact quantum-mechanical iterative fitting procedure. EU = Eigenvalues represent spectroscopic data to within the experimental uncertainties.

²H, there are then four NeH⁺ and six ArH⁺ isotopologues that can be employed to determine unique atom-centered, isotopically invariant BO breakdown functions; with these functions, it is possible to calculate precisely the expected line positions of isotopologues involving the minor isotope ²¹Ne, as well as those of unobserved tritium-containing NeT⁺ and ArT⁺ isotopologues.

There has been one previous study on NeH⁺ [9] that considered the determination of the PEF for the ground electronic state from experimental spectroscopic line position data. The authors employed the Generalized Reduced Potential Curve (GRPC) model and achieved fairly good quality fits, falling just short of consistency with experimental precision. It is believed that the GRPC model probably possesses the required flexibility to reach experimental precision, but in this particular application there was no inclusion of *J*-dependent nonadiabatic effects in the theoretical model. Also, at that time, the total number of available experimental spectroscopic line positions was 122, compared to the 185 line position data employed in the present work.

There have been several past investigations aimed at determining the PEF for the ground electronic state of ArH⁺ by employing experimental spectroscopic line positions [10–17]. The present work is considered a significant advance over all past work in one or more of the following five aspects: (a) it employs the full set of spectroscopic line positions currently available, (b) it considers *J*-dependent nonadiabatic effects, (c) it incorporates the correct long-range functional form of the potentials, employing reliable long-range induction energy coefficients, (d) it involves an exact and fully quantum-mechanical iterative procedure, employing numerical solution of the time-independent radial Schrödinger equation and (e) the quantum-mechanical vibrational-rotational eigenvalues represent the spectroscopic data to within the experimental uncertainties. Table 1 lists these features for all relevant past studies on ArH⁺ and indicates in which way(s) the present work provides improvements over past investigations.

2. Theoretical background

The effective ¹Σ Hamiltonian operator employed in this work was proposed by Coxon [18] on the basis of theoretical work on BO breakdown corrections by Watson [5]. For a heteronuclear diatomic cation AB⁺ for isotopologue *i*, it can be written as,

$$H_i^{\text{AB}^+}(r) = \frac{1}{2\mu_i^{\text{at}}} \nabla_i^2 + V_i^{\text{eff}}(r) + \frac{\hbar^2}{2\mu_i^{\text{at}} r^2} [1 + q_i(r)](J + 1), \quad (1)$$

where $V_i^{\text{eff}}(r)$ is the effective PEF, and $q_i(r)$ represents *J*-dependent nonadiabatic effects. For a charged diatomic cation, the charge-adjusted reduced molecular mass is written as [5],

$$\mu_i^{\text{at}} = \mu_C = \frac{m_i^{\text{A}} m_i^{\text{B}}}{m_i^{\text{A}} + m_i^{\text{B}} - C m_e}, \quad (2)$$

defined in terms of atomic masses m_{A} and m_{B} , the electron mass, m_e , and the total charge, C , on the cationic molecule. The effective PEF can be written as,

$$V_i^{\text{eff}}(r) = V^{\text{BO}}(r) + \frac{m_e}{m_i^{\text{A}}} U^{\text{A}}(r) + \frac{m_e}{m_i^{\text{B}}} U^{\text{B}}(r), \quad (3)$$

where $V^{\text{BO}}(r)$ is the Born-Oppenheimer potential energy, and $U^{\text{A}}(r)$ and $U^{\text{B}}(r)$ are isotopically invariant atom-centered radial functions. These functions comprise the diagonal adiabatic effects as well as homogeneous nonadiabatic effects, combined in a generally undeterminable proportion. The function $q_i(r)$ from Eq. (1) can also be written in a similar way as,

$$q_i(r) = \frac{m_e}{m_i^{\text{A}}} q^{\text{A}}(r) + \frac{m_e}{m_i^{\text{B}}} q^{\text{B}}(r), \quad (4)$$

defined in terms of two isotopically invariant functions $q^{\text{A}}(r)$ and $q^{\text{B}}(r)$ for atomic centers A and B, respectively. These two radial functions contain contributions from homogeneous and heterogeneous nonadiabatic effects that are inseparable when employing field-free data. Isotopic substitution at both atomic centers is required for the unique determination of $V^{\text{BO}}(r)$, $U^{\text{A}}(r)$ and $U^{\text{B}}(r)$. However, this condition is not necessary for a unique determination of both $q^{\text{A}}(r)$ and $q^{\text{B}}(r)$. In this case, isotopic substitution at one atomic center is sufficient. In DPF analyses of this type, the potential function $V^{\text{BO}}(r)$ is not the true BO function, but absorbs nuclear-mass-independent contributions due to relativistic, QED, and finite nuclear volume effects. It is therefore not expected to be in full agreement with accurate ab initio BO calculations. On this point, it is interesting to note that the previously reported experimental “ $V^{\text{BO}}(r)$ ” function of HeH⁺ [7] is actually an effective potential function¹ that does not fully agree with the essentially exact ab initio BO function of Pachucki [19], as shown recently by Tung et al. [8]. The difference function between the Coxon and Hajigeorgiou [7] BO PEF and that of Pachucki [19] summarizes precisely the aforementioned effects, which are normally quite challenging to estimate accurately by ab initio methods, and is thus considered of much value to computational chemists concentrating on this two-electron molecular ion.

It is possible to construct a PEF that is fully consistent with the theoretically predicted limiting form in the long-range region, which can be written according to the second-order perturbation equation [20],

$$V_i^{\text{eff}}(r) = \mathfrak{D}_e - \frac{C_4^{\text{ind}}}{r^4} - \frac{C_6^{\text{ind}}}{r^6} - \frac{C_8^{\text{ind}}}{r^8} - \dots, \quad (5)$$

for the diatomic cations considered in this work. Since the expected dissociation products for both NeH⁺ and ArH⁺ involve a proton (H⁺), the leading interaction term is due to a charge-induced dipole of the rare gas neutral atom. The r^{-6} and r^{-8} terms are due to a charge-induced quadrupole and a charge-induced octupole, respectively. These latter terms, C_6^{ind}/r^6 and C_8^{ind}/r^8 , arise from different interactions than the usual dispersion energy interactions between two neutral atoms that contribute to a long-range PEF.

In modern DPF analyses [21,22], Douketis-type [23] damping functions have been employed to decrease the magnitude of long-range dispersion terms gradually and smoothly with decreasing internuclear separation. The application of damping functions is supported theoretically. It simulates the situation where the two electron clouds begin to penetrate each other, in which case the mutual long-range electron cloud polarizations begin to weaken. From a purely mathematical perspective, if left unrestrained, the r^{-n} terms may create destabilizing effects at short-*r*,

¹ In Ref. [7], in footnote b of Table 1, the value of β_6 should be 0.0406 not 0.406.

causing a fitted PEF inner limb to display pathological behavior. In preliminary work in the present investigation, it was found that inclusion of undamped terms up to C_8^{ind} caused similar significant instability in the short- r portion of the PEF, where the inner limb was found to turn down. This is a physically detrimental result that affects adversely the calculation of energy eigenvalues in a numerical solution of the Schrödinger equation, often causing the least-squares fit to diverge. However, while closed-form mathematical models for damping functions have been developed for dispersion energy terms, we are not aware of any such model for charge-induced energy terms. Even if dispersion damping functions were to be applicable in the present work, simply as an effective way of handling the inner limb problems, these functions cannot be calculated when one of the dissociation products is a hydrogen cation, which lacks electron density. The essential problem is that dispersion damping functions adopted for DPF work involve the atomic first ionization potential in the physical model.

In the present work, we have made use of an ab initio calculation by Wheatley and Meath [24] of induction damping functions for the ions H_2^+ , HeH^+ , and LiH^+ . These functions were listed numerically in succinct tabular form and there was no attempt to provide a general analytical model. Fortunately, it has been found possible in our work to develop closed-form empirical formulas that allow extension to the heavier systems under consideration. It is then possible to modify Eq. (5) as,

$$V_i^{\text{eff}}(r) = \mathfrak{D}_e - D_4^{\text{ind}}(r) \frac{C_4^{\text{ind}}}{r^4} - D_6^{\text{ind}}(r) \frac{C_6^{\text{ind}}}{r^6} - D_8^{\text{ind}}(r) \frac{C_8^{\text{ind}}}{r^8} - \dots, \quad (6)$$

where the terms $D_n^{\text{ind}}(r)$ represent the induction damping functions. The form of these functions is considered in greater detail in Section 3.2.

The theoretical expressions for the C_n^{ind} coefficients in the present case of ion-induced polarizations are given in atomic units as [20],

$$C_n^{\text{ind}} = \frac{\alpha_{\text{pol}}}{2}, \quad (7)$$

where α_{pol} represents the static dipole, quadrupole, and octupole polarizabilities for C_4^{ind} , C_6^{ind} , and C_8^{ind} , respectively. Since the ground state dissociation products of rare gas (RG) hydridic cations (up to Ar, at least) are $\text{RG} + \text{H}^+$, accurate C_n^{ind} coefficients for NeH^+ and ArH^+ were estimated by straightforward scaling of the well-known C_n^{ind} coefficients of HeH^+ , with the relevant static dipole polarizabilities obtained from Ref. [25]. Static quadrupole and octupole polarizabilities for He, Ne, and Ar, required for the calculation of C_6^{ind} and C_8^{ind} for NeH^+ and ArH^+ , were obtained from the calculations of Dalgarno and Victor [26] and Doran [27].

In past work on the two-electron system HeH^+ , Coxon and Hajigeorgiou [7] had discovered that the use of reduced molecular masses calculated from Watson's charge-adjusted prescription, Eq. (2), did not lead to optimum fits. It was reasoned that even in the chemical equilibrium region, the electron cloud distribution was affected by the large difference in the first-ionization energies of He (24.5 eV) and H (13.6 eV), such that helium and hydrogen would not share the two electrons equally. A simple molecular orbital treatment of HeH^+ predicts that the bond order is $\frac{1}{2}$, indicating that only one electron is shared between He and H, while the second electron must be strongly bound to the helium nucleus. This interpretation is further strengthened by the relatively low dissociation energy of HeH^+ , which is less than half of that of the H_2 molecule (bond order = 1), indicating the presence of a weaker-than-normal covalent interaction. Accordingly, Coxon and Hajigeorgiou [7] employed an effective reduced molecular mass attributing 75% of the total electron density to He and only

25% to H. This led to a much improved representation of the spectroscopic data. Owing to the chemical similarity of HeH^+ to the cations NeH^+ and ArH^+ , it was decided to investigate whether various definitions of the reduced molecular mass had any impact on the degree of success of the least-squares fits. For NeH^+ , it was found that the overall most successful reduced mass definition was that of Watson, Eq. (2). For ArH^+ , there was negligible (<0.1%) difference between the standard deviations of fits employing a variety of different reduced mass definitions. This finding is in contrast to the results of a recent [28] multi-isotopologue Dunham analysis of a similar set of ArH^+ spectroscopic transitions; this showed the Watson reduced mass to give noticeably worse results than other options. On the basis of our results, we employed Eq. (2) for both NeH^+ and ArH^+ . Greater detail of these tests is provided in Section 4.

3. Mathematical models

3.1. Potential function and Born-Oppenheimer breakdown functions

In the present work, the core PEF and $q(r)$ functions determined directly are those of the principal (most abundant) isotopologue, instead of the BO PEF. This approach was formulated by Le Roy [29], and is aimed at extracting the most radially extensive functions possible from the spectroscopic data. On the basis of the vibrational extent of the spectroscopic data, we have designated the principal isotopologues as $^{20}\text{NeH}^+$ and $^{40}\text{ArH}^+$. The principal isotopologue PEFs, $V_1^{\text{eff}}(r)$, are modeled by the MLR3 form, which involves a minor modification of the MLR model developed originally by Le Roy and Henderson [30]. The MLR3 model was first employed in an investigation of the Cs_2 ground electronic state [31], and can be written as,

$$V(r) = \mathfrak{D}_e \left[1 - \frac{u_{\text{LR}}(r)}{u_{\text{LR}}(r_e)} e^{-\phi_{\text{MLR3}}(r)y_p(r,r_e)} \right]^2, \quad (8)$$

with

$$u_{\text{LR}}(r) = D_4^{\text{ind}}(r) \frac{C_4^{\text{ind}}}{r^4} + D_6^{\text{ind}}(r) \frac{C_6^{\text{ind}}}{r^6} + D_8^{\text{ind}}(r) \frac{C_8^{\text{ind}}}{r^8}, \quad (9)$$

for the two cations considered in this work, and

$$\phi_{\text{MLR3}}(r) = [1 - y_m(r, r_{\text{ref}})] \sum_{k=0}^N \phi_k y_q(r, r_{\text{ref}})^k + y_m(r, r_{\text{ref}}) \phi(\infty). \quad (10)$$

The three variables employed in Eqs. (8) and (10) above are defined as,

$$y_p(r, r_e) = \left(\frac{r^p - r_e^p}{r^p + r_e^p} \right), \quad y_m(r, r_{\text{ref}}) = \left(\frac{r^m - r_{\text{ref}}^m}{r^m + r_{\text{ref}}^m} \right), \\ y_q(r, r_{\text{ref}}) = \left(\frac{r^q - r_{\text{ref}}^q}{r^q + r_{\text{ref}}^q} \right), \quad (11)$$

where r_{ref} usually takes on values in the range $1.1r_e - 1.5r_e$. Appropriate choice of r_{ref} serves to reduce the order N of the polynomial series in Eq. (10), leading to more economical representations. The limiting value of $\phi(\infty)$ in Eq. (10) can be readily calculated as,

$$\phi(\infty) = \ln \left(\frac{2\mathfrak{D}_e}{u_{\text{LR}}(r_e)} \right). \quad (12)$$

Since the present analysis is not based on a direct application of Eq. (3), it is useful to note the expression that allows for calculation of the minor isotopologue PEFs. This can be written as,

$$V_i^{\text{eff}}(r) = V_1^{\text{eff}}(r) + m_e U^A(r) \left(\frac{1}{m_i^A} - \frac{1}{m_1^A} \right) + m_e U^B(r) \left(\frac{1}{m_i^B} - \frac{1}{m_1^B} \right), \quad (13)$$

It is noted that atomic masses must be employed in applications of Eq. (13). The mathematical model employed to represent the isotopically invariant functions in Eq. (13) is,

$$U^k(r) = u_c^k y_m(r, r_e) + [1 - y_m(r, r_e)] \sum_{i=1}^k u_i^k [y_p(r)]^i, \quad (14)$$

where u_c^k is a large- r limiting constant value, herein constrained to zero, owing to lack of experimental information near the dissociation limit. Since it is well known that the adiabatic correction functions exhibit the same qualitative radial dependence at long-range as that of the PEF [32], it is necessary to constrain the integer m in Eq. (14) to the value of the leading long-range power, $n = 4$. It should be emphasized that although $U^A(r)$ and $U^B(r)$ also include homogeneous ($^1\Sigma \sim ^1\Sigma$) nonadiabatic contributions that do not necessarily display the same radial variation, these are expected to be very small, owing to the large energy separation between the ground $X^1\Sigma^+$ state and the lowest excited $^1\Sigma^+$ state, as discussed later.

The mathematical model employed for the isotopically invariant functions in $q_i(r)$ is defined as,

$$q^k(r) = [1 - y_m(r, r_e)] \sum_{i=1}^k q_i^k [y_p(r)]^i. \quad (15)$$

The function $y_m(r, r_e)$ in Eqs. (14) and (15), which differs from $y_m(r, r_{\text{ref}})$ employed in Eqs. (10) and (11), acts as a switching function, displaying a sigmoidal radial variation. There are no constraints in the value of m in Eq. (15), and different values of m can be employed to vary the rate of switching in optimizing a fit.

3.2. Induction damping functions

Induction energy damping functions have been calculated by Wheatley and Meath [24] for H_2^+ , HeH^+ , and LiH^+ using ab initio methodology; interestingly, it appears that these comprise the only induction damping functions available in the literature. They were reported numerically in Tables 5–7 of Wheatley and Meath [24] for H_2^+ , HeH^+ , and LiH^+ , respectively. For each molecular ion, three damping functions were calculated, namely, $D_4^{\text{ind}}(r)$, $D_6^{\text{ind}}(r)$, and $D_8^{\text{ind}}(r)$. In order to extend these calculations to NeH^+ and ArH^+ , it was necessary to develop analytical models that explore the effect of atomic size on the behavior of such functions. The procedure followed in order to achieve this generalization is described below.

The available induction damping function data were initially represented by,

$$D_n^{\text{ind}}(r) = \exp[-\exp(d_1 - d_2 r)], \quad (16)$$

where r is the internuclear separation, n is the power of the inverse-power induction terms, and the two parameters d_1 and d_2 were determined through a simple nonlinear least-squares fit. Given the three molecular ions and the three induction terms for each ion, this produced a group of nine sets of d_1 and d_2 parameters. The crucial step involved relating the parameters d_1 and d_2 to the atomic size of H, He, and Li. Since the atomic sizes of Ne and Ar lie between those of He and Li, simple interpolation can provide the parameters d_1 and d_2 for these atoms, and this makes the calculation of induction functions for NeH^+ and ArH^+ possible. It was necessary to employ a functional definition of “atomic size” in order to proceed with the modelling of the parameters d_1 and d_2 . The quantity selected to represent this property was the average atomic radius, as estimated from,

$$r_{\text{at}} = \langle r^2 \rangle^{1/2}, \quad (17)$$

Table 2

Estimated parameters of analytical induction damping function models.^a

Molecular ion		$D_4^{\text{ind}}(r)$	$D_6^{\text{ind}}(r)$	$D_8^{\text{ind}}(r)$
H_2^+	d_1	2.377765	2.879636	3.259032
	d_2	2.186389	1.759263	1.507244
HeH^+	d_1	2.286220	2.773619	3.275692
	d_2	3.052324	2.435559	2.154850
LiH^+	d_1	2.687617	3.162691	3.635295
	d_2	1.279403	1.029362	0.928323
NeH^+	d_1	2.289513	2.777625	3.264981
	d_2	3.007660	2.401188	2.118939
ArH^+	d_1	2.389743	2.892564	3.271338
	d_2	2.113812	1.701624	1.455519

^a The coefficients d_1 and d_2 can be employed to calculate the induction damping functions according to Eq. (16), using Å units for the internuclear separation.

obtained by considering the tabulated expectation values of Desclaux [33]. It was found that the dependence of the parameters d_1 and d_2 on the average atomic radius was smooth and slowly varying, enabling reliable interpolations for Ne and Ar. The analytical models adopted for d_1 and d_2 are,

$$d_{nt} = \frac{1}{\rho_{nt1} + \rho_{nt2} r_{\text{at}}^{\rho_{nt3}}}, \quad (18)$$

where the index n refers to the power of the induction term, and the index t refers to the d parameter number. The model is given in terms of the three adjustable parameters ρ_{nt1} , ρ_{nt2} , and ρ_{nt3} , which were determined by application of the simplex method. Table 2 contains the final set of parameters $\{d_1, d_2\}$ for each induction function $D_n^{\text{ind}}(r)$, for the five cationic molecules H_2^+ , HeH^+ , LiH^+ , NeH^+ and ArH^+ . The coefficient set $\{\rho_{nt1}, \rho_{nt2}, \rho_{nt3}\}$, consisting of 18 parameters, is included in Supplementary material as Appendix 1.

4. Application to rare gas hydride cations

The numerical and computational aspects of DPF methodology have been described in detail elsewhere [21]. Briefly, the adjustable parameters of the relevant radial functions are optimized by iterative weighted nonlinear least-squares, employing spectroscopic line positions, with a standard numerical Schrödinger equation solver at the heart of the computer code. The associated Jacobian matrix derivatives are calculated using the Hellmann-Feynman theorem.

The mathematical model adopted for the principal isotopologue PEF is the standard MLR3 form described earlier. A considerable degree of testing is essential in optimizing the models for the various radial functions, particularly with respect to the three powers $\{pmq\}$ in Eq. (11), and the constant r_{ref} in the radial functions $y_m(r, r_{\text{ref}})$ and $y_q(r, r_{\text{ref}})$. The optimization procedure is normally guided to a large extent by minimization of the dimensionless reduced standard deviation of the fit, σ_d ,

$$\sigma_d = \left(\frac{1}{N_d - N_p} \sum_{k=1}^{N_d} \left(\frac{v_{\text{obs}}(k) - v_{\text{calc}}(k)}{\varepsilon(k)} \right)^2 \right)^{1/2}, \quad (19)$$

where $v_{\text{obs}}(k) - v_{\text{calc}}(k)$ and $\varepsilon(k)$ are the residuals and experimental uncertainties, respectively, of the k th transition. N_d is the number of spectroscopic line positions, and N_p is the number of adjustable parameters.

During the fitting stages of the investigations, close attention must be paid to the dimensionless standard deviations of the fits. Blind adherence to this criterion alone, however, can lead to results that are less than optimum, particularly in terms of the physical significance of the derived radial functions. It is crucial to pay close

attention also to the fitted radial form of $\phi_{\text{MLR3}}(r)$ and its concomitant effect on the behavior of the PEF. In some challenging cases, particularly where the experimental data set is scant, pathological behavior in the radial functions beyond the data region can result, even though σ_d alone may indicate a successful fit. The final optimum fits are then usually a compromise between the two factors.

4.1. The ground $X^1\Sigma^+$ electronic state of NeH^+

The spectroscopic data set of NeH^+ employed in the present analysis is derived from six studies [9,34–38]. These single-state data comprise pure rotational and infrared vibrational-rotational spectroscopic line positions that reach up to $v = 4$ for $^{20}\text{NeH}^+$, and cover an energy range of approximately 59% of the dissociation limit. In total, there are 185 available spectroscopic transitions for the four isotopologues $^{20}\text{NeH}^+$ (114), $^{22}\text{NeH}^+$ (22), $^{20}\text{NeD}^+$ (43), and $^{22}\text{NeD}^+$ (6). The large gap in energy up to the dissociation limit suggests that the use of a three-term $u_{\text{LR}}(r)$ function is essential in lending increased physical significance to the extrapolation properties of the PEF beyond the data region.

The 185 spectroscopic transitions for $\text{NeH}^+/\text{NeD}^+$ were reduced to 20 fitted parameters by weighted nonlinear least-squares, giving a dimensionless standard deviation $\sigma_d = 0.9968$, indicating that the model represents the data with precision very close to the experimental uncertainties, on average. As noted earlier, testing of different definitions of the reduced molecular mass was considered, in order to arrive at the best model for the distribution of electron density around the nuclei. For NeH^+ , fits were performed employing five different reduced mass definitions: (a) μ_c , Watson's charge-adjusted reduced mass, Eq. (2), (b) μ_{nuc} , calculated from nuclear masses, (c) μ_{DIS1} , corresponding to the $\text{Ne} + \text{H}^+$ dissociation products, (d) μ_{DIS2} , corresponding to the $\text{Ne}^+ + \text{H}$ dissociation products, and (e) $\mu_{1/2}$, which is associated with the distribution $\text{Ne}^{1/2+} + \text{H}^{1/2+}$. The last definition is consistent with the optimum representation obtained by Coxon and Hajigeorgiou for HeH^+ [7]. The results of our present analysis are summarized in Table 3. It is obvious that use of nuclear masses results in a very inadequate fit, as found also in the initial stages of the HeH^+ work [7]. The range of difference in the other four representations is a mere 0.0194 in the dimensionless root-mean-square (drms) deviation, indicative of fairly similar fit qualities. The best fit was obtained using the reduced mass μ_{DIS2} ($\text{Ne}^+ + \text{H}$), with a $\text{drms} = 0.9428$, but this set of dissociation products is not physically sensible, given the ionization potentials of the constituent atoms. The next best fit was that employing the Watson (μ_c) reduced mass, giving $\text{drms} = 0.9437$, and this representation was therefore adopted for the DPF fit on NeH^+ .

Table 4 lists the estimated least-squares parameters defining the $^{20}\text{NeH}^+$ PEF and Table 5 presents the fitted parameters related to the BO breakdown functions. For each fitted parameter, the number of digits quoted is rounded to the minimum necessary such that all line positions can be regenerated with sufficient precision to give residuals that correspond to the dimensionless standard deviation of the fit. This is achieved with the method of

Table 3
Dimensionless root-mean-square (drms) deviations of DPF fits for a variety of reduced masses.^a

Reduced mass	drms (NeH^+)	drms (ArH^+)
μ_c (Watson)	0.9437	0.7392
μ_{nuc} (nuclear)	3.991	0.7606
μ_{DIS1} ($\text{H}^+ + \text{RG}$)	0.9622	0.7386
μ_{DIS2} ($\text{H} + \text{RG}^+$)	0.9428	0.7393
$\mu_{1/2}$ ($\text{H}^{1/2+} + \text{RG}^{1/2+}$)	0.9506	0.7390

^a Definitions for the various reduced masses are provided in Section 4.1, see text.

Table 4
Estimated MLR3 potential parameters for the optimum DPF fits for $^{20}\text{NeH}^+$ and $^{40}\text{ArH}^+$.^a

	$^{20}\text{NeH}^+$	$^{40}\text{ArH}^+$
r_{min} (Å)	0.60	0.70
r_{max} (Å)	2.60	3.70
Δr (Å)	0.0005	0.0005
p	6	6
m	8	8
q	3	3
r_{ref} (Å)	1.42	1.68
C_4^{ind} ($\text{cm}^{-1} \text{Å}^4$)	2.2910×10^4	9.4960×10^4
C_6^{d} ($\text{cm}^{-1} \text{Å}^6$)	1.6220×10^4	1.2193×10^5
C_8^{ind} ($\text{cm}^{-1} \text{Å}^8$)	2.0497×10^4	3.0356×10^5
\mathfrak{D}_e (cm^{-1})	[18,350]	[32,460]
r_e (Å)	[0.991109]	[1.2803118]
ϕ_0	2.3049500×10^{-3}	8.6216539×10^{-2}
ϕ_1	-1.650731	-2.8168635
ϕ_2	-3.987962	-7.3311094
ϕ_3	-6.61471	-13.762567
ϕ_4	-7.97529	-20.79083
ϕ_5	-7.7661	-27.73858
ϕ_6	-9.898	-33.031
ϕ_7	-17.949	-36.281
ϕ_8	-20.34	-35.413
ϕ_9	-9.1	-28.08
ϕ_{10}		-15.0
ϕ_{11}		-4.0

^a r_{min} and r_{max} are the inner and outer points of integration using a grid size of Δr , for the numerical solution of the radial Schrödinger equation. The integers p , m , and q refer to Eq. (11) and r_{ref} are the pivot points employed in the variables $y_m(r, r_{\text{ref}})$ and $y_q(r, r_{\text{ref}})$ in the same equation. \mathfrak{D}_e are the dissociation energies, constrained to the values given in square brackets. The equilibrium internuclear separations are denoted by r_e and constrained to the values given in square brackets.

Table 5
Estimated Born-Oppenheimer breakdown function parameters for the optimum DPF fits for NeH^+ and ArH^+ .^a

	NeH^+	ArH^+
$U^{\text{H}}(r)$		
NS:NL	2:4	3:4
p	4	2
m	4	4
$m_e u_c$	[0.0]	[0.0]
$m_e u_1$	13.08	14.37
$m_e u_2$	-11.50	-77.4
$m_e u_3$	-65.0	12.0
$m_e u_4$	70.0	-480.0
$U^{\text{RG}}(r)$		
NS:NL	2:2	2:2
p	2	2
m	4	4
$m_e u_c$	[0.0]	[0.0]
$m_e u_1$	69.8	102.0
$m_e u_2$	80.0	20.0
$q^{\text{H}}(r)$		
NS:NL	3:3	2:2
p	1	1
m	2	3
$m_e q_1$	[0.0]	1.1×10^{-4}
$m_e q_2$	6.0×10^{-3}	-8.0×10^{-4}
$m_e q_3$	-1.0×10^{-2}	
$q^{\text{RG}}(r)$		
NS:NL		1:1
p		1
m		3
$m_e q_1$		-1.0×10^{-3}

^a NS and NL are the highest powers of the polynomial expansions for the $r < r_e$ and $r > r_e$ regions of the radial functions, respectively. Parameter estimates appearing in square brackets were constrained to the values given inside the square brackets.

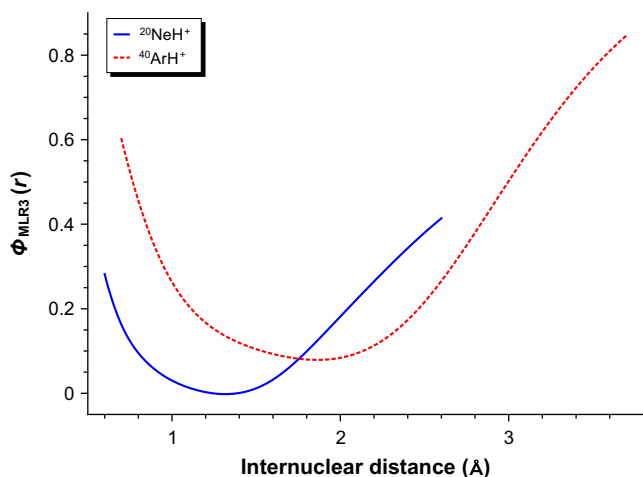


Fig. 1. The fitted $\phi_{\text{MLR3}}(r)$ radial functions for the ground $X^1\Sigma^+$ electronic states of $^{20}\text{NeH}^+$ and $^{40}\text{ArH}^+$. The functions are calculated from the fitted ϕ_i parameters listed in Table 4 and Eqs. (10) and (11), see text.

sequential rounding described by Le Roy [39]. Fig. 1, shows the $\phi_{\text{MLR3}}(r)$ function of the principal isotopologue, $^{20}\text{NeH}^+$, employing a $\{pmq\} = \{683\}$ representation. Fig. 1 also displays the equivalent fitted function for $^{40}\text{ArH}^+$, which is the principal isotopologue of ArH^+ , the analysis of which is considered in Section 4.2. Table 6 lists the quantum-mechanical vibrational eigenvalues and the corresponding “turning points” of the principal isotopologue PEF. We have deposited as Supplementary materials: (a) Appendix 2: tables that contain RKR-style PEFs for all other isotopologues of NeH^+ included in the fitting procedure, (b) Appendix 3: tables containing vibrational term values, rotational and centrifugal distortion constants for all isotopologues included in the fit, and (c) Appendix 4: the full results of our least-squares fit.

4.2. The ground $X^1\Sigma^+$ electronic state of ArH^+

The experimental spectroscopic data base employed in the determination of radial functions for ArH^+ consists of the spectroscopic transitions employed by Coxon and Molski [15], and in addition includes the recent data from Ref. [28]. This data set includes $X^1\Sigma^+$ state information that extends up to $v = 7$ for the principal isotopologue, $^{40}\text{ArH}^+$, with vibrational energy approximately equal to 53% of the dissociation energy. In total, there are 458 spectroscopic transitions for the six isotopologues, $^{40}\text{ArH}^+$ (374), $^{40}\text{ArD}^+$ (54), $^{36}\text{ArH}^+$ (21), $^{38}\text{ArH}^+$ (7), $^{36}\text{ArD}^+$ (1), and $^{38}\text{ArD}^+$ (1). The optimization of the mathematical model for the principal isotopologue PEF was achieved in a manner similar to that described above for NeH^+ , employing a $\{pmq\} = \{683\}$ representation for the radial function $\phi_{\text{MLR3}}(r)$ in Eq. (8), the same as that employed for NeH^+ .

Least-squares fits were performed for five different reduced masses, as explained above for NeH^+ . Table 3 summarizes the key information related to this analysis. It is evident that employing the nuclear masses leads to the most unsatisfactory fit. The other four fits resulted in drms values that were very close to each other, the maximum difference being 0.0007 in the drms. On the basis of the results in Table 3, and for the sake of consistency, the Watson’s charge-adjusted reduced mass, Eq. (2), was employed for this molecular ion as well. It is not entirely clear why our result for the Watson reduced mass, μ_c , differs from the result obtained in Ref. [28], for a multi-isotopologue fit of Dunham coefficients.

The 458 spectroscopic line positions were included in a least-squares fit to the physical model having 23 adjustable parameters, and giving a dimensionless standard deviation $\sigma_d = 0.7589$. This indicates that the assignments of experimental uncertainties to the spectroscopic data were to some extent pessimistic for the majority of the data. Tables 4 and 5 list the estimates of the parameters considered in the least-squares fit to the effective PEF for $^{40}\text{ArH}^+$, as well as auxiliary functions that allow the principal isotopologue functions to be transformed to those of minor isotopologues. Table 6 gives an RKR-style PEF for the principal isotopologue. Fig. 1 displays the $\phi_{\text{MLR3}}(r)$ function of $^{40}\text{ArH}^+$. In the Supplementary materials, we include: (a) Appendix 5: RKR-style PEFs for all isotopologues included in the least-squares fits, (b) Appendix 6: vibrational term values, rotational and centrifugal distortion constants for these isotopologues, and (c) Appendix 7: the full results of the least-squares fit.

5. Discussion

5.1. The potential energy functions

Fig. 1, given earlier in this article, displays the radial behavior of the $\phi_{\text{MLR3}}(r)$ functions for the principal isotopologues $^{20}\text{NeH}^+$ and $^{40}\text{ArH}^+$, and hence also to a large extent the radial variations of the PEFs for these two molecules. Although the magnitudes of these functions are somewhat different, the general inner and outer limb radial variations have distinct similarities. Fig. 2, which shows the reduced PEFs for HeH^+ , $^{20}\text{NeH}^+$ and $^{40}\text{ArH}^+$, also indicates that their behavior is comparable. The broad resemblance in the radial behavior of these functions validates the conclusion that similar effects control the formation and chemical behavior of the protonated RG = He, Ne, Ar bonding interactions.

Theoretical chemists have contributed to the understanding of the bonding forces involved for the RG-hydridic cations, by performing rather accurate calculations of the PEFs of NeH^+ and ArH^+ . In recent work, Gerivani et al. [40] carried out MRCI calculations of several electronic states of NeH^+ . The ground electronic state potential was calculated in the range 0.7–15.0 a.u. at 50 different internuclear separations. Moreover, these authors demonstrated convincingly that the long-range portion of their function follows the expected C_4^{ind}/r^4 dependence at large internuclear

Table 6
RKR-style listings of the potential energy functions for the ground $X^1\Sigma^+$ electronic states of $^{20}\text{NeH}^+$ and $^{40}\text{ArH}^+$.

v	$^{20}\text{NeH}^+$			$^{40}\text{ArH}^+$		
	G_v (cm^{-1})	r_{min} (Å)	r_{max} (Å)	G_v (cm^{-1})	r_{min} (Å)	r_{max} (Å)
0	1426.871	0.895714	1.119570	1341.89741	1.179473	1.406731
1	4104.728	0.841750	1.242958	3931.17711	1.118745	1.519862
2	6558.143	0.811009	1.348547	6401.65786	1.082382	1.610462
3	8788.645	0.789537	1.451651	8756.21482	1.055778	1.693258
4	10795.876	0.77341	1.55802	10997.59384	1.034761	1.772564
5				13128.3649	1.017450	1.850430
6				15150.8702	1.002814	1.928096
7				17067.1628	0.990220	2.006455

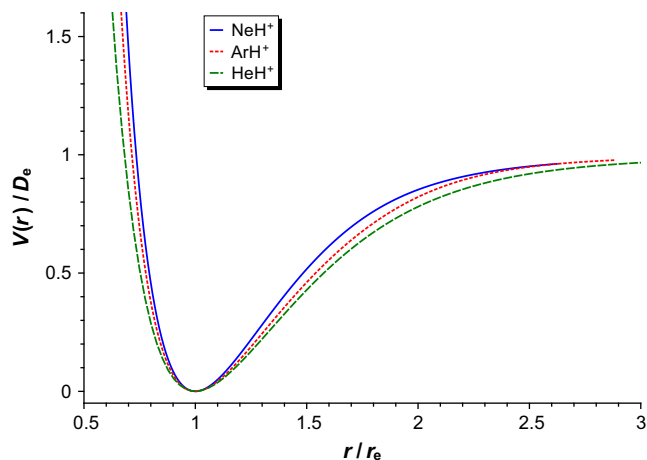


Fig. 2. Reduced potential energy functions, $V(r)/D_e$, for HeH^+ (green long dashes), NeH^+ (blue solid line), and ArH^+ (red short dashes) plotted as functions of r/r_e . The potential energy functions for NeH^+ and ArH^+ are from the present work and that for HeH^+ is from Ref. [7]. (For interpretation of the references to color in this figure legend, the reader is referred to the web version of this article.)

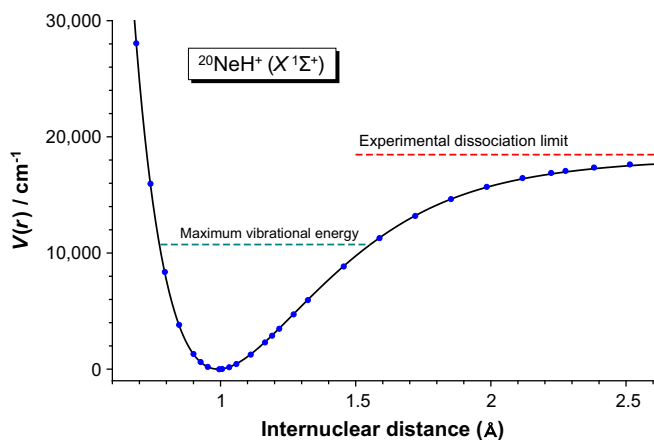


Fig. 3. Potential energy function for $^{20}\text{NeH}^+$. The solid black line represents the fitted MLR3 function from the present work, and the blue solid circles represent points from the ab initio function of Ref. [40]. The red dashed line signifies the experimental dissociation energy, and the green dashed line the highest vibrational energy (59% of D_e) sampled by the experimental data. (For interpretation of the references to color in this figure legend, the reader is referred to the web version of this article.)

spacings, which is indicative of the reliability and accuracy of their function. In Fig. 3, we compare the MLR3 fitted PEF to the ab initio function of Ref. [40]. The dissociation energy of the ab initio function is $D_e = 18,449 \text{ cm}^{-1}$, whereas the MLR3 function constrained the dissociation energy to the experimental value $D_e = 18,350 \text{ cm}^{-1}$ [41]. The agreement between the two functions is considered very satisfactory.

The most accurate calculation of the ground electronic state of ArH^+ has been carried out by Stolyarov and Child [42]. These authors employed the multireference averaged quadratic coupled cluster method (MR-AQCC) to produce PEFs for the ground and low-lying excited states having Σ and Π character. The coupled cluster method, while computationally more demanding, is widely recognized for giving more accurate theoretical results. The comparison between the MLR3 PEF from the present work, and the ground state PEF from Ref. [42] is shown in Fig. 4. Although the quoted dissociation energy is $D_e = 4.14 \text{ eV}$ ($33,392 \text{ cm}^{-1}$), careful application of numerical methods on the reported ab initio PEF points [42] has been able to determine that the dissociation

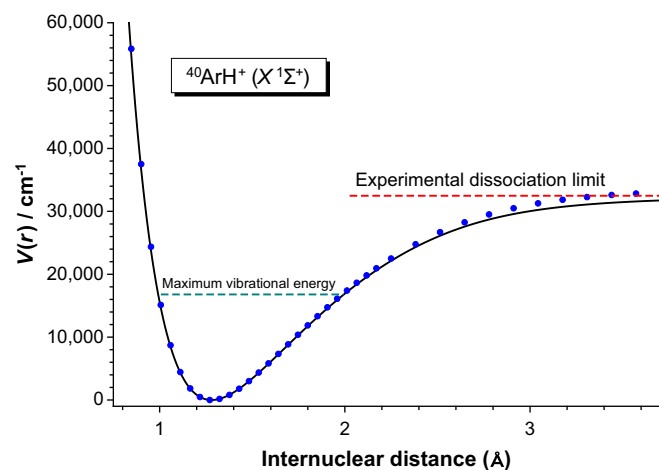


Fig. 4. Potential energy function for $^{40}\text{ArH}^+$. The solid black line represents the fitted MLR3 function from the present work, and the blue solid circles represent points from the ab initio function of Ref. [42]. The red dashed line signifies the experimental dissociation energy, and the green dashed line the highest vibrational energy (53% of D_e) sampled by the experimental data. (For interpretation of the references to color in this figure legend, the reader is referred to the web version of this article.)

energy of the theoretical curve is closer to $D_e = 0.15398 \text{ a.u.}$ ($33,796 \text{ cm}^{-1}$). This is different by 1336 cm^{-1} from the experimental dissociation energy we employed as a constrained parameter in our DPF fit, $D_e = 32,460 \text{ cm}^{-1}$ [41]. The agreement between the two functions is very good at lower energies, but there are visible differences on the outer limb at higher energies. The difference between the experimental and theoretical dissociation energies for NeH^+ is only of the order of 0.5%, whereas for ArH^+ the analogous difference exceeds 4%. Given that the ArH^+ theoretical calculations [42] were performed at the accurate coupled-cluster level, it may be necessary to resolve this issue by making more precise experimental measurements of the ground state dissociation limit.

The least-squares fits provided highly precise estimates for the equilibrium internuclear separations of the potential functions for the ground $X^1\Sigma^+$ electronic states of the principal isotopologues $^{20}\text{NeH}^+$ and $^{40}\text{ArH}^+$. We obtained the estimate $r_e = 0.991109(2) \text{ \AA}$ for $^{20}\text{NeH}^+$. There is significant disagreement between our estimate and the value $r_e = 0.991160(2) \text{ \AA}$ calculated from the Dunham coefficient Y_{01} obtained in 2004 [9], as well as with the experimental value $r_e = 0.991154(2) \text{ \AA}$ from a 1998 microwave study [37]. The estimate $r_e = 1.28031178(6) \text{ \AA}$ obtained in the present study for $^{40}\text{ArH}^+$, is in significant disagreement with the 2014 value $r_e = 1.28032979(13) \text{ \AA}$ obtained in Ref. [28]. This type of discrepancy is not surprising. The experimental values were determined using Dunham's theoretical framework [43], and need to be adjusted by the semiclassical correction in order to be comparable with the estimates obtained in the present work. The Dunham coefficient Y_{01} needs to be corrected according to Watson's prescription [44],

$$Y_{01} = \frac{\hbar^2}{2\mu r_e^2} \left\{ 1 + \frac{\Delta Y_{01}^D}{B_e} \right\}, \quad (20)$$

where $B_e \approx Y_{01}$, and the semiclassical (Dunham) correction is given as,

$$\Delta Y_{01}^D = \frac{B_e^3}{4\omega_e^2} \{30 + 28a_1 + 21a_1^2 + 21a_1^3 - 18a_2 - 46a_1a_2 + 30a_3\}, \quad (21)$$

where $\omega_e \approx Y_{10}$, and the a_i are Dunham potential constants. These potential constants were obtained for NeH^+ and ArH^+ by fitting

the near-minimum regions of the MLR3 potentials to the Dunham potential model [43]. The Y_{01} coefficient from Ref. [9] for NeH^+ was corrected and this gave $r_e = 0.991134(2) \text{ \AA}$ which now compares better with the MLR3 estimate $r_e = 0.991109(2) \text{ \AA}$. The Y_{01} coefficient from Ref. [28] for ArH^+ was corrected and this gave $r_e = 1.28032098(13) \text{ \AA}$ which now compares better with the MLR3 estimate $r_e = 1.28031178(6) \text{ \AA}$. While it is evident that improvement was achieved in obtaining agreement between the present MLR3 estimates and the best semiclassically corrected experimental values, there are still residual differences that are statistically significant. These residuals may arise from model error in both the present DPF potentials and the experimental Y_{01} estimates, but also from the fact that the MLR3 estimates intrinsically include QED and relativistic effects. It is very difficult to estimate the required corrections to Y_{01} from such effects as there has been no theoretical work that considers these.

5.2. Born-Oppenheimer breakdown and radial functions

Fig. 5 shows the $m_e U^H(r)$ BO breakdown functions for the ground electronic states of NeH^+ and ArH^+ . The x -coordinate is the ratio r/r_e , which ensures that both functions bisect the x -axis at the same point, allowing for a more direct comparison of the radial dependence of the two functions. There is a general similarity in the radial behavior of the two functions, although there are significant differences in their magnitudes. A similar plot of the functions $m_e U^{\text{RG}}(r)$ for the rare gas atoms Ne/Ar is shown in Fig. 6. It can be seen that the two functions behave in a remarkably similar fashion. This can be interpreted as confirmation of the similarity in the arrangements of the electronic state manifold for the two molecular ions. According to Watson [5], the $U^k(r)$ functions can be expressed as,

$$U^k(r) = \tilde{S}^k(r) = S^k(r) + \frac{1}{2} \left(\frac{dV^{\text{BO}}(r)}{dr} \right) \int Q^k(r) dr \quad (22)$$

where the $S^k(r)$ represent individual atomic contributions to the diagonal (adiabatic) correction function, and the $Q^k(r)$ functions represent homogeneous nonadiabatic coupling effects. In the theoretical study of the ArH^+ ground and excited electronic states, Stoljarov and Child [42] mapped precisely the electronic state manifold involving singlet and triplet Σ and Π states (see Fig. 1 of this

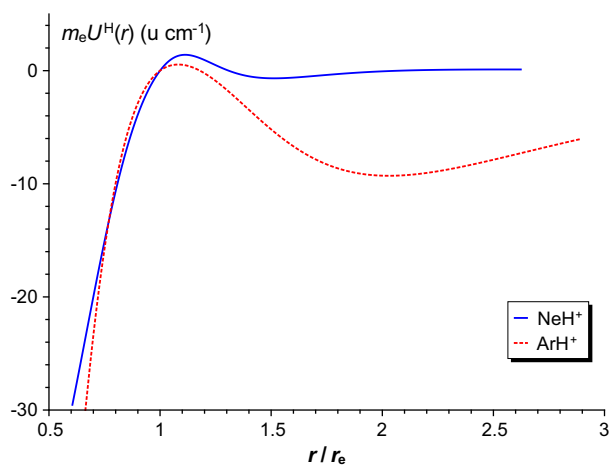


Fig. 5. The fitted $m_e U^H(r)$ radial functions for the ground $X^1\Sigma^+$ electronic states of NeH^+ (solid blue line) and ArH^+ (dashed red line). The radial functions are calculated from the parameters listed in Table 5 and Eqs. (11) and (14). (For interpretation of the references to color in this figure legend, the reader is referred to the web version of this article.)

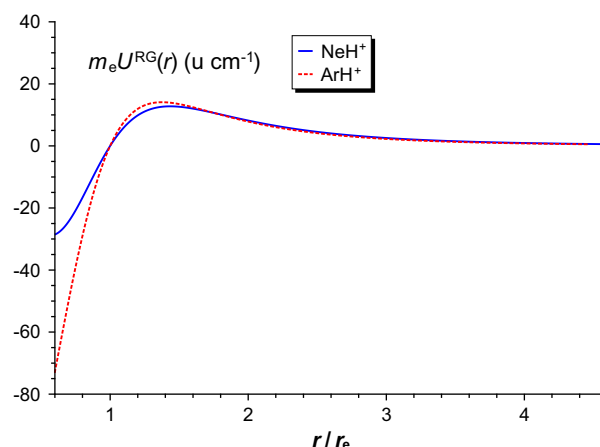


Fig. 6. The fitted $m_e U^{\text{RG}}(r)$ radial functions for the ground $X^1\Sigma^+$ electronic states of NeH^+ (solid blue line) and ArH^+ (dashed red line). The radial functions are calculated from the parameters listed in Table 5 and Eqs. (11) and (14). (For interpretation of the references to color in this figure legend, the reader is referred to the web version of this article.)

article). The vibrational-rotational energy levels of the ground $X^1\Sigma^+$ electronic state are expected to couple homogeneously to the repulsive $A^1\Sigma^+$ ($\sim 70,000 \text{ cm}^{-1}$) and weakly bound $C^1\Sigma^+$ ($\sim 120,000 \text{ cm}^{-1}$) excited electronic states. A similar state of affairs is expected with regard to the arrangement of electronic states for NeH^+ . This accounts for the similarity in the radial behavior of the functions in Figs. 5 and 6. The second-order perturbation coupling matrix elements depend indirectly on the electronic state separations, and given the relatively high energies of these excited $^1\Sigma^+$ states, homogeneous nonadiabatic effects on the ground state are expected to be of small magnitude. It is therefore very probable that the adiabatic approximation holds relatively well for the $X^1\Sigma^+$ electronic state, albeit any attempt to represent highly precise spectroscopic data without explicit consideration of nonadiabatic contributions would fail, as has been verified for HeH^+ [7].

Corresponding plots of the $q^k(r)$ functions defined by the parameters in Table 5 are not shown. The parameters of these functions were determined with low statistical significance, and their radial variations are believed to be reliable only near the region of the PEF equilibrium internuclear separation. These functions describe J -dependent nonadiabatic perturbations on the ground $X^1\Sigma^+$ electronic states of the two molecular cations. Watson [5] showed that these functions derive contributions from pure $\Sigma \sim \Pi$ heterogeneous nonadiabatic coupling effects, as well as $\Sigma \sim \Sigma$ homogeneous nonadiabatic interactions. The experimentally sampled rotational levels of the ground electronic state are expected to couple through a heterogeneous channel to the repulsive $B^1\Pi$ ($\sim 50,000 \text{ cm}^{-1}$) and the weakly bound $D^1\Pi$ ($\sim 115,000 \text{ cm}^{-1}$) excited electronic states. Any effects on the rotational levels of the ground $X^1\Sigma^+$ electronic state are then likely to arise mostly from the less distant $B^1\Pi$ repulsive state, but the effects are not expected to be particularly large. This is confirmed when examining the very small magnitude of the fitted $q^k(r)$ radial functions, for which only 1–2 fitted parameters could be determined, and even then, with fairly low statistical significance. Coxon and Hajigeorgiou [7] encountered very similar circumstances in fitting spectroscopic line positions of the HeH^+ isotopologues, obtaining a two-term small-magnitude hydrogenic function, while an analogous rare gas function was not statistically supported. There is no question that inclusion of these terms is required to provide a satisfactory fit of the spectroscopic data. However, it is not prudent to place much significance on their radial variations, as they

are likely reliable only over a small range of r near the potential minimum. In order to obtain better statistical significance for the $q^k(r)$ functions, highly excited vibrational and rotational levels need to be sampled experimentally, for both NeH^+ and ArH^+ . This can only come about from the spectroscopic investigation of electric-dipole allowed electronic transitions to the ground $X^1\Sigma^+$ state. The anticipated electronic transitions, however, would fall into the vacuum-uv part of the spectrum, and this would pose a number of experimental challenges.

5.3. Calculation of radial functions

In our recent analysis of the hydrogen halides [21], the [Supplementary materials](#) included a Fortran computer code for calculation of the various radial functions obtained in the DPF procedure from the tabulated fitted parameters. A representative data file for HF was also provided, in order to assist with the use of the computer code. Investigators interested in calculating the radial functions for NeH^+ and ArH^+ obtained in the present work, need only modify the HF data file provided, using the results presented in [Tables 4 and 5](#).

6. Conclusions

In the present work, DPF methodology was employed in analyzing all the spectroscopic line positions available on the ground $X^1\Sigma^+$ electronic states of the rare gas hydride cations, NeH^+ and ArH^+ . Precise determinations of the PEFs for the principal isotopologues $^{20}\text{NeH}^+$ and $^{40}\text{ArH}^+$ have been achieved, along with radial functions describing BO breakdown effects, and which enable the calculation of the analogous functions for other isotopologues of these astrophysically important molecules. Comparisons made with available ab initio PEF functions suggest that experimental determinations of the dissociation energies \mathcal{D}_e need to be made with higher accuracy, particularly for ArH^+ , where there is considerable disparity with theoretical results, as well as significant disagreement amongst the available experimental measurements. Also, there is a need to study the higher vibrational levels for both molecules, in order to determine J -dependent nonadiabatic effects with higher statistical significance. Finally, DPF analyses for the heavier cations KrH^+ and XeH^+ should be carried out, in order to complete the investigations on this family of interesting molecular ions.

Note added in proof

We thank Dr. Holger Müller (Universität zu Köln) for bringing our attention to the recent work of Luca Bizzocchi and coworkers on the first microwave spectra of $^{36}\text{ArH}^+$ and $^{38}\text{ArH}^+$ (Astronomical Journal Letters, 820 (2016) L26). These authors obtained precise measurements of the $J = 1 \leftarrow 0$ transitions as 617525.149 ± 0.020 and 6166648.707 ± 0.020 for $^{36}\text{ArH}^+$ and $^{38}\text{ArH}^+$, respectively. It is a very noteworthy indication of the power of DPF methodology that these transitions are calculated from the parameters in [Tables 4 and 5](#) of the present work as 617525.171 and 616648.713 MHz, differing by only 0.022 and 0.006 MHz, respectively, from the experimental values. It is remarkable that such agreement, essentially within the estimated experimental error, is achieved without any microwave data for $^{36}\text{ArH}^+$ and $^{38}\text{ArH}^+$ in the present data set. Similarly, our calculations for $^{36}\text{ArH}^+$ of transitions up to $J = 4 \leftarrow 3$, and of the $P(14)$ through $P(20)$ lines of the 1–0 band, are in close (but poorer) agreement the predictions of Bizzocchi et al. For the

1–0 transitions, for example, our predictions range from about 0.002 to 0.01 cm^{-1} less than those of Bizzocchi et al. over $P(14)$ through $P(20)$.

Acknowledgments

PGH thanks the School of Medicine, University of Nicosia for support of this work. The authors wish to thank Prof. Robert J. Le Roy for helpful correspondence, and dedicate this article to him for his significant contributions to the field of diatomic spectroscopic analysis.

Appendix A. Supplementary material

Supplementary data associated with this article can be found, in the online version, at <http://dx.doi.org/10.1016/j.jms.2016.08.002>.

References

- [1] M. Born, J.R. Oppenheimer, *Ann. Phys.* 389 (1927) 457–484.
- [2] N.C. Handy, A.M. Lee, *Chem. Phys. Lett.* 252 (1996) 425–430.
- [3] R.M. Herman, A. Asgharian, *J. Mol. Spectrosc.* 19 (1966) 305–324.
- [4] P.R. Bunker, R.E. Moss, *Mol. Phys.* 33 (1977) 417–424.
- [5] J.K.G. Watson, *J. Mol. Spectrosc.* 80 (1980) 411–421.
- [6] R.M. Herman, J.F. Ogilvie, *Adv. Chem. Phys.* 103 (1998) 187–215.
- [7] J.A. Coxon, P.G. Hajigeorgiou, *J. Mol. Spectrosc.* 193 (1999) 306–318.
- [8] W.-C. Tung, M. Pavanello, L. Adamowicz, *J. Chem. Phys.* 137 (2012) 164305.
- [9] S. Civiš, J. Šebera, V. Špirko, J. Fišer, W.P. Kraemer, K. Kawaguchi, *J. Mol. Struct.* 695–696 (2004) 5–11.
- [10] M. Gruebele, E. Keim, A. Stein, R.J. Saykally, *J. Mol. Spectrosc.* 131 (1988) 343–366.
- [11] J.F. Ogilvie, *J. Mol. Spectrosc.* 156 (1992) 8–14.
- [12] A. Šurkus, *Chem. Phys. Lett.* 279 (1997) 236–240.
- [13] A. Šurkus, *Spectrochim. Acta A* 56 (2000) 1979–1981.
- [14] M. Molski, *Chem. Phys. Lett.* 342 (2001) 293–298.
- [15] J.A. Coxon, M. Molski, *J. Mol. Spectrosc.* 223 (2004) 51–66.
- [16] A.D. Smirnov, *Opt. Spectrosc.* 98 (2005) 485–489.
- [17] M. Rey, V.G. Tyuterev, J.A. Coxon, R.J. Le Roy, *J. Mol. Spectrosc.* 238 (2006) 260–263.
- [18] J.A. Coxon, *J. Mol. Spectrosc.* 117 (1986) 361–387.
- [19] K. Pachucki, *Phys. Rev. A* 85 (2012) 042511.
- [20] G.C. Maitland, M. Rigby, E.B. Smith, W.A. Wakeham, *Intermolecular Forces – Their Origin and Determination*, Clarendon Press, Oxford, 1981.
- [21] J.A. Coxon, P.G. Hajigeorgiou, *J. Quant. Spectrosc. Radiat. Transfer* 151 (2015) 133–154.
- [22] Y.-S. Cho, R.J. Le Roy, *J. Chem. Phys.* 144 (2016) 024311.
- [23] C. Douketis, G. Scoles, S. Marchetti, M. Zen, A.J. Thakkar, *J. Chem. Phys.* 76 (1982) 3057–3063.
- [24] R.J. Wheatley, W.J. Meath, *Chem. Phys.* 179 (1994) 341–364.
- [25] The CTCP Table of Experimental and Calculated Static Dipole Polarizabilities for the Electronic Ground States of the Neutral Elements, Centre for Theoretical Chemistry and Physics, New Zealand Institute for Advanced Study, Massey University, New Zealand <<http://ctcp.massey.ac.nz/index.php?menu=dipole&page=dipole>>.
- [26] A. Dalgarno, G.A. Victor, *Proc. Phys. Soc. Lond.* 90 (1967) 605–608.
- [27] M.B. Doran, *J. Phys. B* 7 (1974) 558–569.
- [28] M. Cueto, J. Cernicharo, M.J. Barlow, B.M. Swinyard, V.J. Herrero, I. Tanarro, J.L. Doménech, *Astrophys. J. Lett.* 783 (2014) L5.
- [29] R.J. Le Roy, *J. Mol. Spectrosc.* 194 (1999) 189–196.
- [30] R.J. Le Roy, R.D.E. Henderson, *Mol. Phys.* 105 (2007) 663–677.
- [31] J.A. Coxon, P.G. Hajigeorgiou, *J. Chem. Phys.* 132 (2010) 094105.
- [32] M. Przybytek, B. Jeziorski, *Chem. Phys.* 401 (2012) 170–179.
- [33] J.P. Desclaux, *Atom. Data Nucl. Data* 12 (1973) 311–406.
- [34] M. Wong, P. Bernath, T. Amano, *J. Chem. Phys.* 77 (1982) 693–696.
- [35] R.S. Ram, P.F. Bernath, J.W. Brault, *J. Mol. Spectrosc.* 113 (1985) 451–457.
- [36] D.-J. Liu, W.-C. Ho, T. Oka, *J. Chem. Phys.* 87 (1987) 2442–2446.
- [37] F. Matsushima, Y. Ohtaki, O. Torige, K. Tagaki, *J. Chem. Phys.* 109 (1998) 2242–2245.
- [38] W.J. Ting, T. Amano, *Chin. J. Phys.* 52 (2014) 1248–1276.
- [39] R.J. Le Roy, *J. Mol. Spectrosc.* 191 (1998) 223–231.
- [40] B. Gerivani, A. Shayesteh, A. Maghari, *Comp. Theor. Chem.* 1070 (2015) 82–87.
- [41] H. Hotop, T.E. Roth, M.-W. Ruf, A.J. Yencha, *Theor. Chem. Acc.* 100 (1998) 36–50.
- [42] A.V. Stolyarov, M.S. Child, *Phys. Chem. Chem. Phys.* 7 (2005) 2259–2265.
- [43] J.L. Dunham, *Phys. Rev.* 41 (1932) 721–731.
- [44] J.K.G. Watson, *J. Mol. Spectrosc.* 45 (1973) 99–113.